The 9th European Congress on Computational Methods in Applied Sciences and Engineering
ECCOMAS Congress 2024
3–7 June 2024, Lisboa, Portugal

EXPERIMENTAL AND NUMERICAL CHARACTERIZATION OF THE DISCHARGE FLOW OF LOW-PRESSURE ROTOR-ONLY AXIAL FANS

H. Witte[1,2], C. Bode[1]

[1] Institute of Jet Propulsion and Turbomachinery, Technische Universität Braunschweig, Hermann-Blenk-Str. 37, 38108 Braunschweig

[2] Corresponding author: h.witte@tu-braunschweig.de

Key words: Low-pressure rotor-only axial fans, Delayed detached eddy simulation, Particle image velocimetry

Summary. In this work, a newly designed low-pressure rotor-only axial fan was manufactured and subsequently investigated experimentally and numerically. For the experimental investigation, five-hole-probe and particle image velocimetry measurements of the fan discharge flow were performed. The results of this investigation are used to validate numerical simulations. Three different simulation setups of varying fidelity from industry-standard RANS simulations to non-zonal delayed detached eddy simulations (DDES) were performed. The comparison shows that RANS simulations deviate strongly from the experimental results. Also the utilization of a full Reynolds stress turbulence model does not improve the results. The DDES on the other hand shows significantly better agreement with the experimental data while only moderately increasing the computational effort.

1 Introduction

Supplying high volumetric flow rates while maintaining relatively small pressure ratios, low-pressure axial fans find use in a broad range of applications. Typical examples include ventilation of tunnels or metro stations, heat pumps, air conditioning or active cooling towers. Due to cost and space constraints or the necessity to allow for reversing operation, these types of fans are often installed without outlet guide vanes (OGVs) and discharge directly into a free atmosphere. Consequently, the discharged jet features a strong circumferential velocity component. Considering the isentropic simple radial equilibrium, this velocity component through inertial forces results in a sub-atmospheric static pressure immediately downstream of the trailing edge of the fan. Due to mixing with the surrounding air and eventually dissipation, the cirucmferential velocity component of the discharge flow is vanishing in the streamwise direction and the static pressure is therefore approaching the atmospheric level. This effectively results in a static pressure increase in the free atmosphere which is comparable to the static pressure recovery that is usually achieved in OGVs. Since for these type of fans, the total-static efficiency computed with the downstream static pressure defined as the ambient pressure is the relevant metric to evaluate the full energy conversion process of the the machine, this static pressure recovery is directly impacting the fan efficiency: Increasing the static pressure recovery, while keeping constant the hydraulic efficiency and the exit loss of the fan would result directly in an increase of

fan efficiency. Previous investigations have shown, that under the simplifying assumptions implied by the isentropic simple radial equilibrium (no streamline curvature and no viscous forces in particular), the fan efficiency can vary up to 8 % through the choice of the vortex design alone [1]. However, in a subsequent study it was observed, that the streamline curvature and the viscous forces do have a significant (negative) impact on the static pressure recovery and consequently on the fan efficiency [2]. It is thus important to understand and control the impact of the fan design on these quantities as well as on the inertial forces, such that the static pressure recovery can be fully taken advantage of. However, since the streamline curvature and the viscous forces especially are difficult to measure, these investigations rely heavily on numerical simulations. The scope of this work is the experimental validation of such numerical simulations using five-hole-probe (5HP) measurements and particle-image-velocimetry (PIV).

2 Methodology

2.1 Fan design

The fan investigated in this study was designed with an in-house design tool described in [2] and [3]. The operating point and geometric boundary conditions of the fan design are listed in table 1.

Table 1: Operating point and geometric boundary conditions for the fan design

Flow coefficient φ	0.215
Total-total work coefficient ψ_t	0.300
Total-static work coefficient $\psi_t s$	0.215
Tip radius r_{tip}	0.2485 m
Rotational speed n	22.5 Hz
Hub-to-tip ratio ν	0.5
Tip gap	0.0015 m
Slope of the linear work distribution k_y	141,4 m/s^2
Number of blades	5

The first step in the fan design is the definition of the vortex design in terms of a linear radial work distribution as in

$$Y(r) = k_y \cdot r + k_\psi. \tag{1}$$

The constant k_ψ is iterated until the desired (total-total) flow coefficient ψ is reached. The value of the constant k_y as listed in table 1 is chosen to yield an optimal static pressure recovery using the methodology described in [1]. Applying the Euler equation and the isentropic simple radial equilibrium, the radial profiles of the circumferential and axial velocity component can be computed from the given work distribution through:

$$c_u(r) = \frac{Y(r)}{2 \cdot \pi \cdot n \cdot r} = \frac{k_y}{2 \cdot \pi \cdot n} + \frac{k_\psi}{2 \cdot \pi \cdot n \cdot r} \qquad \text{and} \tag{2}$$

$$c_x(r) = \sqrt{2 \cdot \left(k_y \cdot r - \frac{k_y^2}{4 \cdot \pi^2 \cdot n^2} \cdot \ln(r) + \frac{k_y \cdot k_\psi}{4 \cdot \pi^2 \cdot n^2 \cdot r} \right) + k_\varphi}. \tag{3}$$

Here, the additional constant k_φ is iterated until the desired flow coefficient φ is reached. With the velocity vectors known over the span, the blade angles are derived in the blade-to-blade plane by applying the well-known Weinig method [4], which is based on a conformal mapping approach for non-profiled blades. The resulting blade geometry is manufactured through a stereo-lithography 3D-printing process. The blade root is designed to be clamped between an up- and downstream hub plate as seen in a CAD-model in figure 1a. Figure 1b shows a picture of the manufactured and assembled fan.

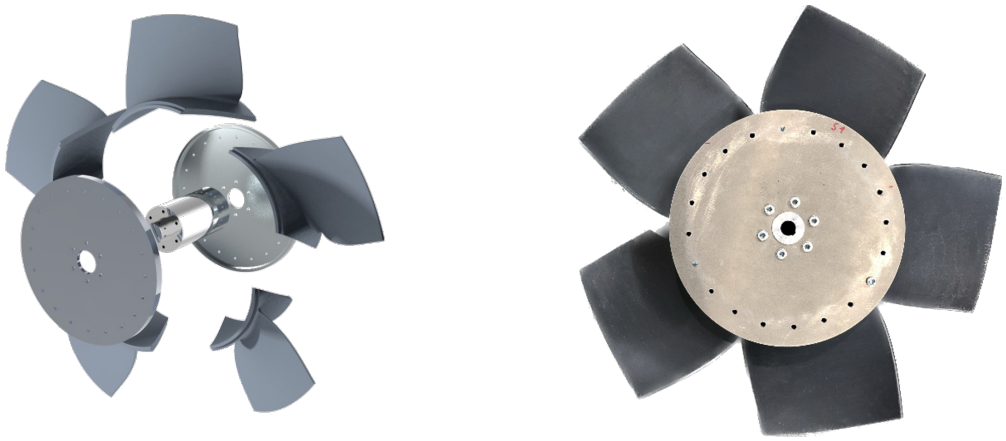

(a) CAD-model (b) Assembled fan

Figure 1: Modular fan design with 3D-printed blades

2.2 Experimental setup

The fan is investigated in an inlet-side chamber test bench for performance measurement in accordance with ISO 5801 [5]. It is installed in a free inlet and free outlet configuration and the operating point is set to the design conditions listed in table 1. Figure 2 shows a sketch of the test bench. The volumetric flow rate is measured at the inlet nozzle. The auxiliary fan and the throttle allow for an adjustment of the fan operating point in terms of volumentric flow rate and pressure ratio. The flow straightener assures a low inflow turbulence to the tested fan. At the drive train, the torque applied to the fan shaft is measured and with the rotational speed, the input power is computed. The input power is then corrected to account for the mechanical loss within the drive train. In the upstream test chamber the (average) total pressure is measured. Together with the available ambient pressure, the total-static fan pressure can be computed.

A five-hole-probe (5HP) specifically designed for this investigation is used to measure the radial velocity profiles immediately downstream of the trailing edge still inside fan annulus. The measurement plane of the 5HP is located 9 mm upstream of the hub edge and is marked in figure 3b. Due to the high pneumatic inertia of the 5HP measurement system including tubes and pressure transducers, no time resolving measurements are possible. Instead, circumferentially and temporally averaged results are generated by recording 200 measurements for a fixed position of the probe and varying relative position of the fan and subsequent arithmetic averaging.

The discharge flow of the fan is measured with a stereo (3D2C) PIV-setup. Two HiSense

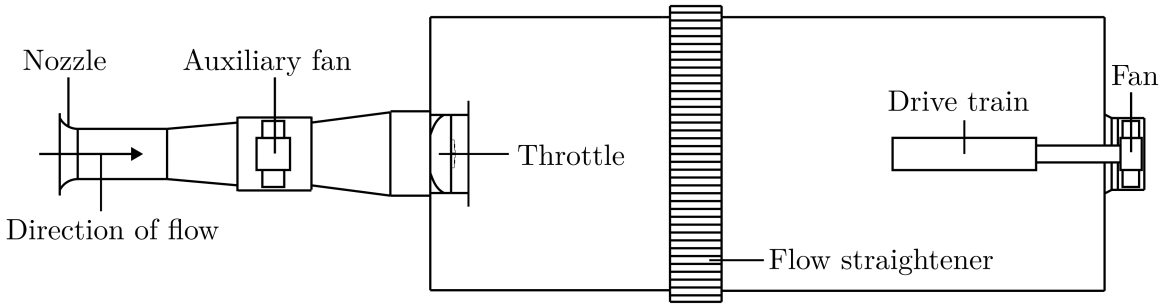

Figure 2: Sketch of the chamber test bench

Mk I cameras from Dantec Dynamics, each equipped with a AF Nikkor lens from Nikon, were used. The technical specifications of the cameras and lenses are listed in table 2. The lenses were opened to the maximum aperture during the measurements. Figure 3a schematically shows the arrangement of the cameras relative to the fan and the laser sheet in a aft-looking-forward view. The laser used for this study is a two cavity Nd:YAG laser of the type Gemini from New Wave Research. Its specifications are also listed in table 2. The seeding of the flow was realized with a a Unique 2.1 Hazer from Look Solutions positioned upstream of the inlet nozzle. Both cameras are mounted on a traversing system, allowing the measurement area to be shifted in the axial and radial direction without the need for re-calibration. Figure 3b shows a sketch of a meridional view of the setup. The target area of the PIV investigations is outlined in red. Since the measurement area for a fixed position of the cameras is much smaller, than the target area, ten individual measurement areas are defined and the cameras are positioned accordingly with the traversing system for each area. In the post-processing, the individual measurement areas are merged by means of linear interpolation in the overlapping regions. Due to the low pulse frequency of the laser and the low maximum frame rate of the cameras, time resolved measurements were not feasible. Additionally, the laser pulses and camera frames were not triggered by the angular position of the fan and thus, no spatially resolved measurements (relative to the fan) were done either. Instead, by setting the pulse and camera frequency to 3,63 Hz (the fan revolves with 22.5 Hz, thus the greatest common divisor is small) and by recording and subsequent averaging 96 vector fields, a spatial and temporal average of the discharge flow was measured. The transformation of the raw double pictures into the vector fields was done with the "Adaptive PIV" method of the DynamicStudio software by Dantec Dynamics. To average the 96 vector fields, the method "Vector Statistics" was used. The interpolation of the ten individual measurement areas was done with an in-house Python tool.

2.3 Numerical setup

Figure 4 shows a meridional slice of the computational domain with the contour of the instantaneous axial velocity. Upstream of the fan, a small section of the chamber of the test bench is included in the domain. Downstream of the fan a large plenum representing the free atmosphere is making up the largest part of the domain. The extensions of both sections up- and downstream of the fan have been gradually increased, until the results were not impacted

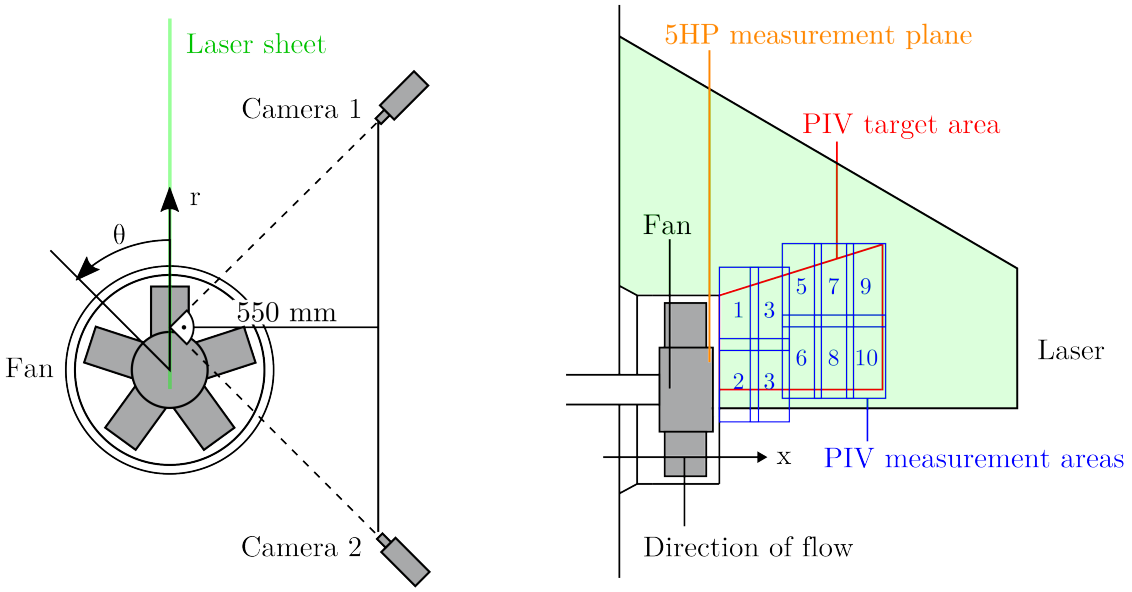

(a) Aft-looking-forward view

(b) Meridional view

Figure 3: Sketch of the experimental setup

anymore. At both the inlet upstream of the fan as well as the inlet to the large plenum (secondary inlet), total flow quantities, flow direction and turbulence quantities are prescribed. At the outlet, the static pressure is set to ambient pressure. All aerodynamic boundary conditions are listed in table 3. The imprinted pressures at the inlets and the outlet correspond to the experimental operating point. The surfaces enveloping the upstream section and the large plenum are modeled as inviscid wall. All other surfaces are either smooth solid walls or moving smooth solid walls (surfaces of the fan itself) with cell sizes of $y^+ \approx 1$. To utilize the symmetry of the geometry only one fifth - one blade passage - of the full 360 deg domain was simulated. The resulting mesh has around $1 \cdot 10^6$ cells.

In this work, three different numerical approaches have been investigated. The set of governing equations for each setup is derived from a finite volume approach with a varying order of

Table 2: Specifications of the used hardware

Cameras	
Resolution	1280 x 1024 Px
Sensor size	6.7 x 6.7 μm
Maximum frame rate	9 Hz

Camera lenses	
Focal length	28 mm
Maximum aperture	1 : 2.8
Minimum aperture	1 : 22

Laser	
Wave length	532 nm
Pulse energy	100 mJ
Pulse frequency	15 Hz
Pulse duration	4 ns
Ray diameter	4.5 mm

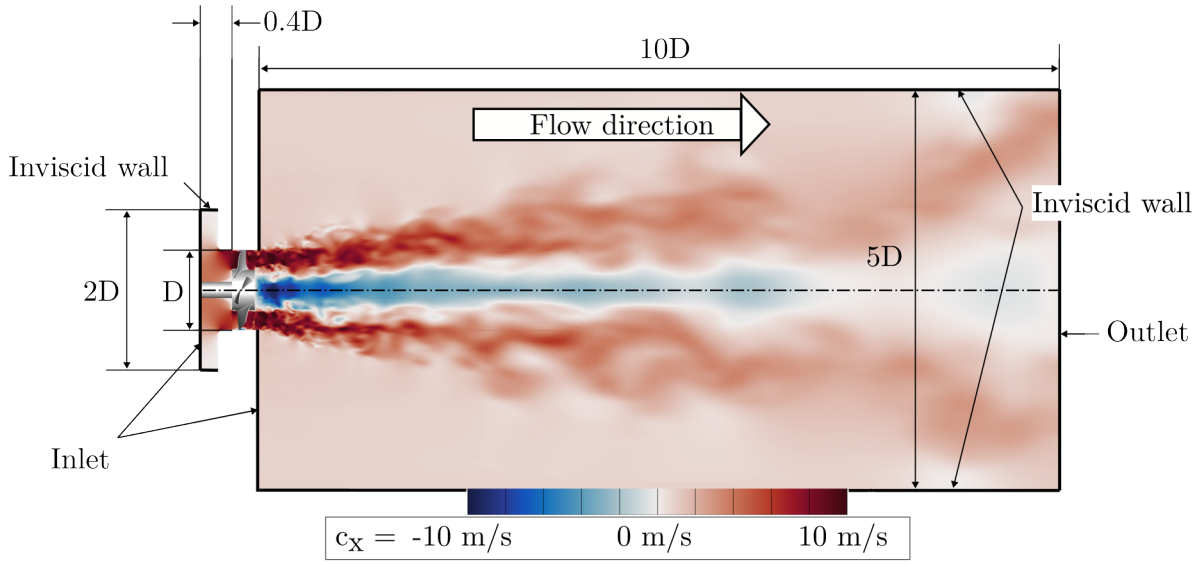

Figure 4: Meridional slice of the instantaneous axial velocity c_x and the numerical and geometrical boundary conditions.

Table 3: Aerodynamic boundary conditions of the numerical setup

Location	Total pressure	Total temp.	Flow direction	Turbulence intensity	Turbulent length scale	Static pressure
Upstream inlet	101176 Pa	300 K	Axial	0.5 %	4 mm	-
Secondary inlet	101325 Pa	300 K	Axial	0.5 %	4 mm	-
Outlet	-	-	-	-	-	101325 Pa

accuracy depending on the turbulence modeling approach. Three different turbulence modeling approaches with increasing fidelity have been investigated. All approaches are applied to the same numerical mesh. The first approach is a standard RANS-setup which can be described as a well-established baseline for industrial applications. Here, the two equation eddy viscosity turbulence model known as the k-ω-SST turbulence model described by Menter in [6] is used. Additionally, to account for laminar turbulent transition, the γ model described in [7] is used. This setup is a steady simulation using a second order Fromm scheme for the spatial discretization with a van Albada Limiter. The second turbulence modeling approach is RANS-Reynolds-Stress. Here, the spatial discretization scheme is the same as in the RANS-setup and the simulation is steady state as well. However, as turbulence model the stress transport model called Wilcox-stress-ω-model [8] consisting of a set of six equations for the Reynolds stress tensor is used. For the highest fidelity level investigated in this work, a non-zonal delayed detached eddy simulation (DDES) approach is chosen. The DDES method is based on the detached eddy simulation (DES) approach as described be Strelets in [9]. The subsequent DDES formulation is a modification of this approach to tackle the modeled-stress-depletion problem. In this work,

the DDES formulation based on the k-ω-SST turbulence model (analogue to the RANS-setup) as described by Gritskevich [10] is used. For this approach, the destruction term of the transport equation of the turbulent kinetic energy is defined with a modified length scale:

$$D_{k,DDES} = \frac{\rho k^{\frac{3}{2}}}{l - f_d \max\left(0, l - C_{DES}\Delta_{DES}\right)}. \tag{4}$$

If the term $l - C_{DES}\Delta_{DES}$ is below zero, the model falls back to the standard formulation of the k-ω-SST turbulence model. However, if this term is larger than zero (or the turbulent length scale of the original model l is larger than $C_{DES}\Delta_{DES}$), $C_{DES}\Delta_{DES}$ becomes the active length scale. If $C_{DES}\Delta_{DES}$ is small, the destruction term becomes large, resulting in a destruction of the modeled turbulent kinetic energy. The parameter C_{DES} depends on the spatial discretization scheme. For the parameter Δ_{DES} on the other hand, a formulation based on the local vorticity vector as described by Shur et al. in [11] is used. The factor f_d works similar to the shielding function of the original formulation of the k-ω-SST turbulence model and delays $C_{DES}\Delta_{DES}$ being the active length scale, giving the DDES its name. To be consistent with the RANS setup, the γ transition model is also used for the DDES. For the DDES setup, a spatial discretization of third order accuracy is used. Additionally, since the DDES is an unsteady simulation, an Euler backwards formulation with second order accuracy is chosen. The time stepping size is set to 100 time steps per period (per 1/5th revolution of the fan) with 30 sub-iterations in a dual time-stepping approach. TRACE is used as flow solver, which is developed by the German Aerospace Center (DLR) [12].

3 Results and discussion

3.1 Velocity profiles

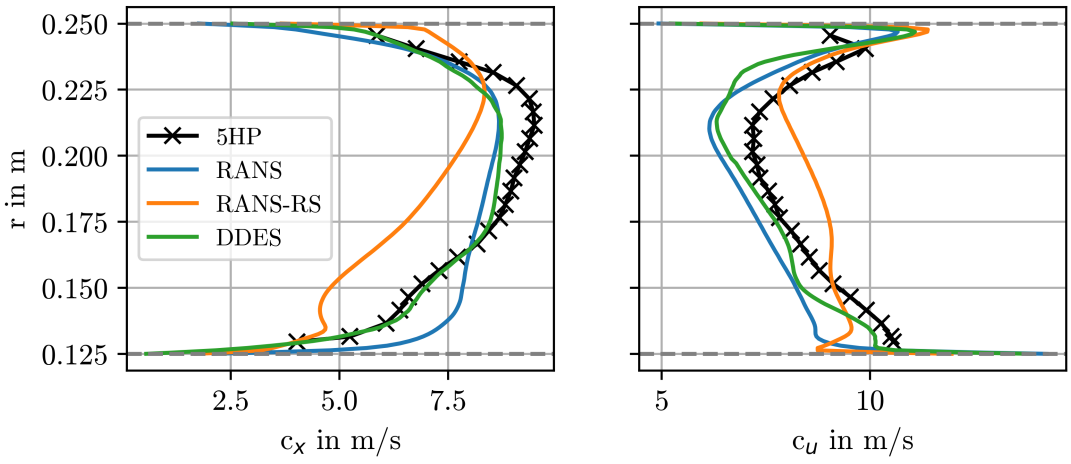

Figure 5: Radial profiles of the axial velocity c_x and absolute circumferential velocity c_u

Figure 5 shows the results of the 5HP measurements compared to the numerical results. The gray dashed lines mark the hub and shroud radius. The results of the numerical setups differ

significantly. The RANS overestimates the axial velocity c_x close to the hub, while the RANS-Reynolds stress setup significantly underestimates it almost over the full radius. In terms of the axial velocity profile, the DDES agrees very well with the experimental data, especially close to the hub. Only the peak value close to the casing is not matched well. The deviations between the measurements and the simulations with respect to c_x also reveal, that the operating point is not matching: While the total-static pressure increase and thus the corresponding work coefficient are inherently equal between CFD and experiment due to the given boundary conditions of the numerical setup, the volumetric flow rate and thus the flow coefficient are varying. For the RANS setup, the overestimation of axial velocity at the hub is somewhat compensated through a underestimation close to the casing. For the RANS-Reynolds setup on the other hand, the volumetric flow rate is significantly lower than in the experiment. The DDES matches the volumetric flow rate best of the investigated setups. The overall trend of the deviations between experiment and numerics seen for c_x also is present for the absolute circumferential velocity c_u. The larger incidence angle due to the overall lower axial velocity in the RANS-Reynolds stress setup leads to the fact, that the flow deflection is overestimated, resulting in an overestimation of c_u over most of the span. The RANS-setup underestimates the flow deflection on the other hand. The match between experimental and numerical data is best for the DDES.

3.2 Velocity contours

Figure 6 shows contours of experimental (PIV) and numerical results of the absolute circumferential velocity c_u. As described in section 2.2, the results are circumferentially and temporally averaged. The position of the fan and the hub are marked with the white and black rectangle respectively. Due to a combination of very low velocities and low seeding particle density outside of the discharge flow, the pictured section of the PIV results is limited to flow regions inside of the discharge flow and does not extend beyond the shear layers. A first observation of figure 6 is that the numerical results strongly differ between the three investigated setups: Only the RANS-setup shows high circumferential velocities close to the hub. The RANS-Reynolds stress setup on the other hand, shows remarkably low values of c_u at the hub region. The DDES shows the best agreement to the PIV-results.

Analogue to figure 6, figure 7 shows contour plots of the axial velocity c_x. The general trend seen for c_u also extends to c_x: The RANS-setup shows high axial velocities close to the hub and is seemingly not able to depict the extension of the re-circulation region into the fan annulus. Due the axial velocity being more evenly distributed over the radius, the peak values are also significantly lower than in the PIV results, i.e. the velocity profile is more flat in the RANS-setup. For the RANS-Reynolds stress setup on the other hand, the opposite of this effect is true: The re-circulation area is inflated and consequently the peak axial velocity in the outer regions of the discharged jet is exaggerated compared to the experimental results. Again, the DDES agrees best with the experimental results. An equivalent trend is also true for the mixing behaviour of the discharged jet: The decay of the peak axial velocity and the associated radial expansion of the jet in the axial direction of the DDES is close to what is seen in the experimental results. For both the RANS and the RANS-Reynolds stress, the mixing deviates from the PIV data. In the RANS case, the expansion of the jet is excessive, while the RANS-Reynolds stress underestimates it.

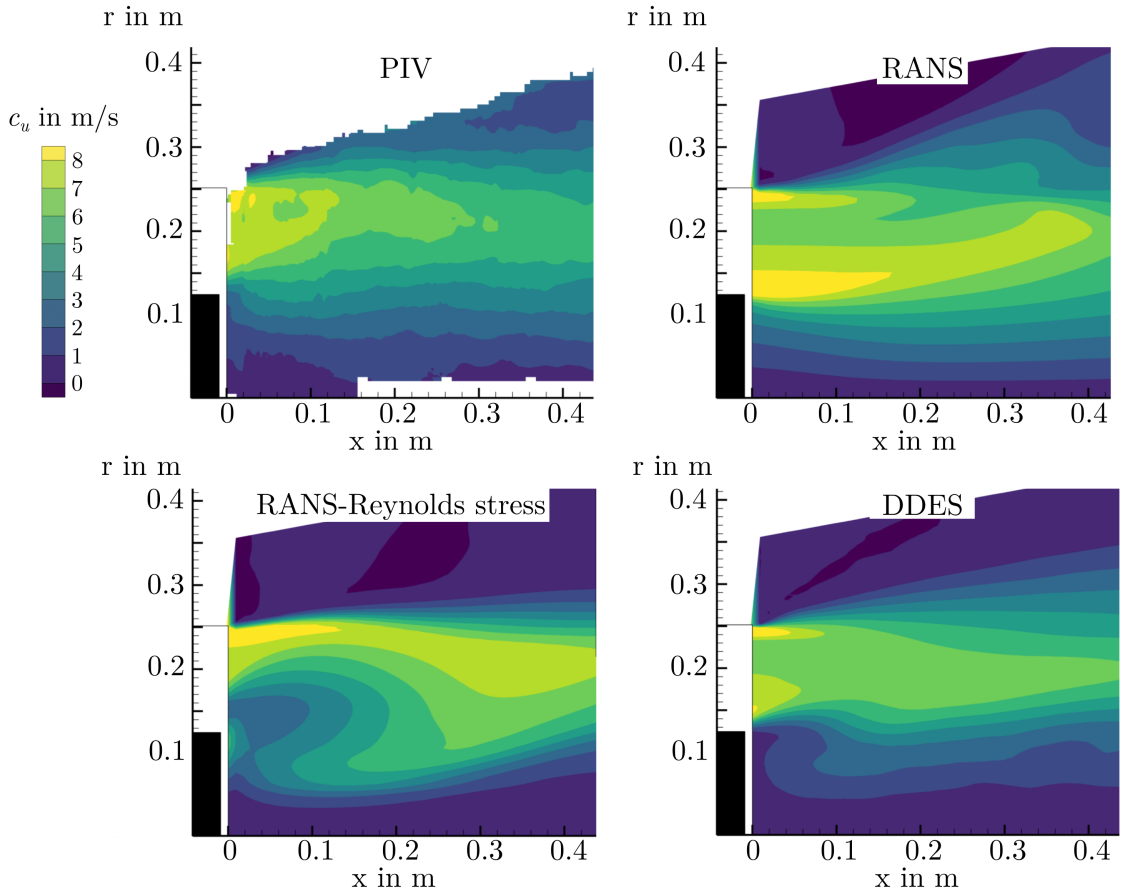

Figure 6: Contour plots of the circumferential and temporal average of the absolute circumferential velocity c_u

3.3 Turbulence intensity

In addition to the (averaged) velocity vectors, the turbulence intensity is a result of the statistical analysis of the 96 recorded vector fields of the PIV measurements. Figure 8 shows radial profiles of the turbulence intensity at varying axial positions downstream of the fan. The axial positions given in the title of the individual plots is defined such that an axial position of 0 corresponds to the edge of the casing - analogue to the x-coordinate shown in figures 6 and 7. For the numerical results, the turbulence intensity is computed through

$$Tu = \frac{\sqrt{\frac{2}{3}k}}{c}, \tag{5}$$

where c is the magnitude of the velocity vector. In the case of the RANS and RANS-Reynolds stress setup, the turbulent kinetic energy k is the modeled quantity. For the DDES setup, k is the sum of the modeled and resolved parts of turbulence. It is apparent, the RANS setup with a standard two-equation eddy viscosity modeling approach fails to depict the behavior of the turbulence intensity close to the core of the discharge flow ($r \to 0$). Here, the Tu shows excessive

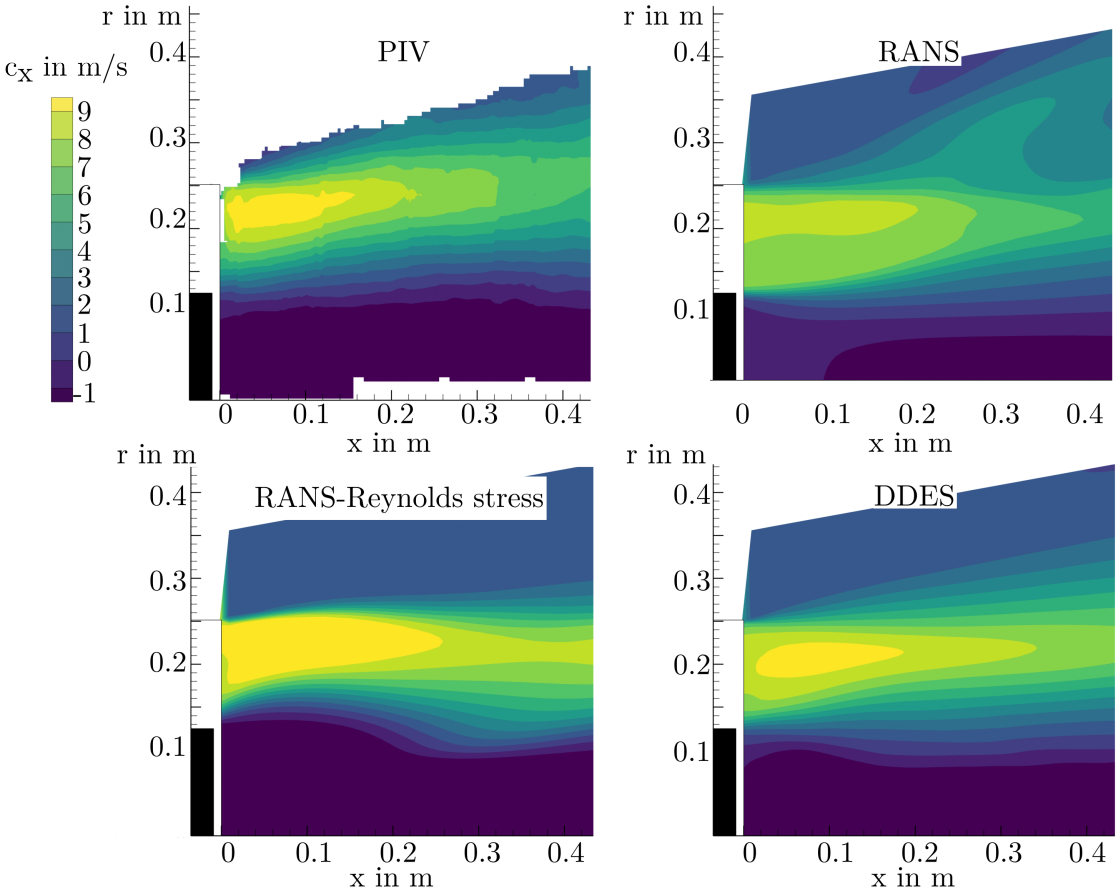

Figure 7: Contour plots of the circumferential and temporal average of c_x

values exceeding 100 %. On the other hand, the RANS setup underestimates Tu in the flow regions of higher velocity at $r \approx 0.2$ m. While the RANS-Reynolds stress agrees better with the experimental data than the RANS setup, is still shows significant deficiencies. Especially the radial expansion of the upper peak in Tu from $r \approx 0.275$ m at $x = 0.1$ m to $r \approx 0.375$ m at $x = 0.4$ m is not captured at all by the RANS-Reynolds setup. Again, the DDES setup, while still showing deviations, agrees best with the experimental data.

4 Conclusions and outlook

The combination of five-hole-probe and PIV measurements conducted in this work yield a extensive database for the validation of numerical simulations. A set of three numerical setups with varying turbulence modeling approaches but unchanged numerical meshes was investigated and held against the experimental data. The choice of the turbulence modeling significantly effects the quality of the results. From the three tested setups, steady RANS setup with a standard two-equation eddy viscosity turbulence model (k-ω-SST) was computationally the most efficient. However, the deviation between the results of this setup and the experimental data overshadows the computational efficiency. The deficits of the RANS setup are primarily but not

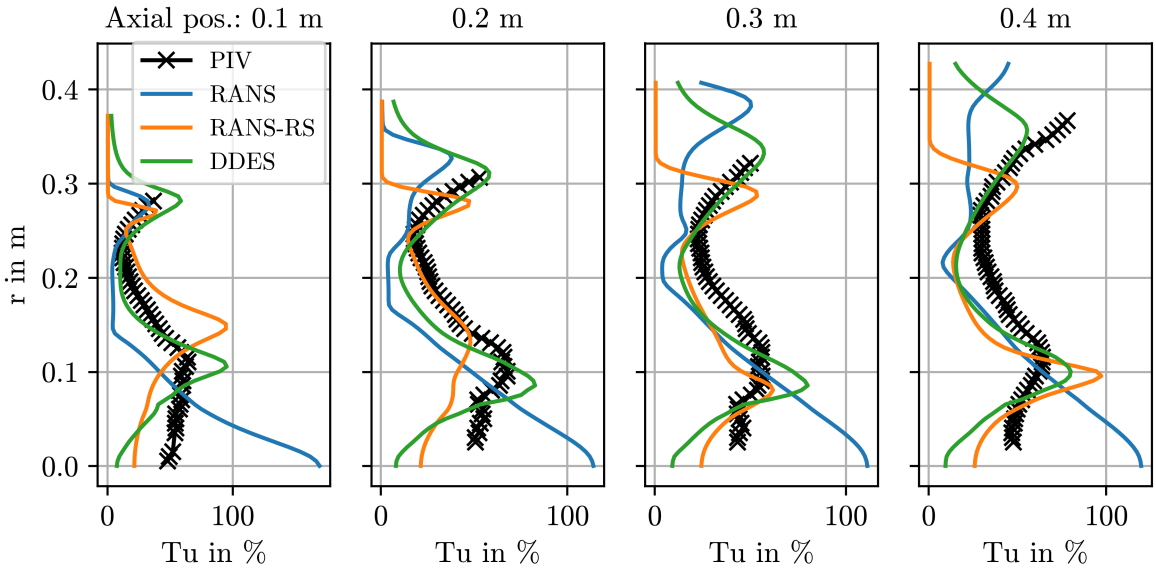

Figure 8: Profiles of the turbulence intensity at different axial positions downstream of the fan

exclusively located at the hub region and towards the core of the discharged jet flow. The RANS setup does not depict, a flow separation in the fan annulus close to the hub region. Additionally, the turbulence intensity is massively overestimated in the core region of the discharge flow, while being underestimated in other regions of the flow. For the investigated RANS-Reynolds stress setup, the full Reynolds stress model called Wilcox-stress-ω was used. The increase of computational effort with respect to the standard RANS setup is mild. However, the results do not significantly improve. In fact, some flow features not seen in the RANS setup (e.g. hub separation) are present but strongly exaggerated, effectively yielding larger deviations from the experimental data. The third numerical setup, that was investigated in this work used a DDES non-zonal approach based on the the k-ω-SST eddy viscosity model. The computational effort increases significantly for this setup, since opposed to the RANS setups, this is an unsteady simulation with relatively small time steps. However, the results match the experimental data well. To further understand and validate the resolution of the turbulence in the DDES setup, time resolved experimental data (e.g. hot-wire measurements) are required. Additionally, a comparison to a fully resolved LES could help to further understand and evaluate the impact of the size the turbulent spectrum and to derive more general statements regarding the required temporal and spatial resolution of a RANS-LES hybrid setup such as DDES.

Acknowledgments

This research was partially funded by the Forschungsvereinigung für Luft- und Trocknungstechnik (FLT) (IGF-Nr. 59 EWN). The FLT is part of the German Federation of Industrial Research Associations (AiF), and the projects are financed by the German Federal Ministry for Economic Affairs and Climate Action (BMWK). The authors gratefully acknowledge the computing time made available to them on the high-performance computer "Lise" at the NHR Center NHR@ZIB. This center is jointly supported by the Federal Ministry of Education and Research

and the state governments participating in the NHR (www.nhr-verein.de/unsere-partner).

REFERENCES

[1] Witte, Hauke, Bode, Christoph and Friedrichs, Jens. "Potential of Static Pressure Recovery of Rotor-Only Low-Pressure Axial Fans." *International Journal of Turbomachinery, Propulsion and Power* Vol. 8 No. 3 (2023). DOI 10.3390/ijtpp8030033.

[2] Witte, Hauke and Bode, Christoph. "Impact of Blade Design on Static Pressure Recovery of Rotor-Only Low-Pressure Axial Fans." *Submitted to: Proceedings of the ASME2024 Fluids Engineering Division Summer Meeting FEDSM2024, July 15-17, Anaheim California* (2024).

[3] Lindemann, Thore Bastian, Friedrichs, Jens and Stark, Udo. "Development of a New Design Method for High Efficiency Swept Low Pressure Axial Fans With Small Hub/Tip Ratio." *Volume 1A: Aircraft Engine; Fans and Blowers*. 2014. American Society of Mechanical Engineers, Düsseldorf, Germany. DOI 10.1115/GT2014-25932.

[4] Weinig, Fritz. "Die Strömung um die Schaufeln von Turbomaschinen." *Johann Ambrosius Barth, Leipzig* (1935).

[5] ISO. *5801:2017; Fans - Performance testing using standardized airways*. International Organization for Standardization, Geneva, Switzerland (2018).

[6] Menter, F R, Kuntz, M and Langtry, R. "Ten Years of Industrial Experience with the SST Turbulence Model." *Heat and Mass Transfer* Vol. 4 (2003).

[7] Menter, Florian R., Smirnov, Pavel E., Liu, Tao and Avancha, Ravikanth. "A One-Equation Local Correlation-Based Transition Model." *Flow, Turbulence and Combustion* Vol. 95 No. 4 (2015). DOI 10.1007/s10494-015-9622-4.

[8] Wilcox, David C. *Turbulence Modeling for CFD*, 3rd ed. DCW Industries, La Canada, CA (2006).

[9] Strelets, M. "Detached eddy simulation of massively separated flows." *39th Aerospace Sciences Meeting and Exhibit*. 2001. American Institute of Aeronautics and Astronautics, Reno,NV,U.S.A. DOI 10.2514/6.2001-879.

[10] Gritskevich, Mikhail S., Garbaruk, Andrey V., Schütze, Jochen and Menter, Florian R. "Development of DDES and IDDES Formulations for the k-ω Shear Stress Transport Model." *Flow, Turbulence and Combustion* Vol. 88 No. 3 (2012). DOI 10.1007/s10494-011-9378-4.

[11] Shur, Mikhail L., Spalart, Philippe R., Strelets, Mikhail Kh. and Travin, Andrey K. "An Enhanced Version of DES with Rapid Transition from RANS to LES in Separated Flows." *Flow, Turbulence and Combustion* Vol. 95 No. 4 (2015). DOI 10.1007/s10494-015-9618-0.

[12] German Aerospace Center (DLR). "CFD Framework TRACE." `https://www.dlr.de/en/at/research-transfer/software/cfd-framework-trace`. Accessed: 30-08-2024.